The Effectiveness of Grain Refinement by Machine Hammer Peening in High Deposition Rate Wire-Arc AM Ti-6Al-4V

J.R. HÖNNIGE, A.E. DAVIS, A. HO, J.R. KENNEDY, L. NETO, P. PRANGNELL, and S. WILLIAMS

Surface deformation, applied in-process by machine hammer peening (MHP), has the potential to refine the coarse columnar β-grain structures normally found in high deposition rate Wire-Arc Additive Manufacturing (WAAM) processes with Ti alloys like Ti-6Al-4V. Effective refinement, as well as a reduction in texture strength, has been achieved in relatively thick sections and to a depth that is greater than that expected from the surface deformation induced by MHP. By application of MHP to each deposition track, the average β-grain size could be reduced from cm's to less than 0.5 mm. Systematic experiments have been performed to investigate the origin of this interesting effect, which included 'stop-action' trials and separation of the strain and temperature gradients induced by the two process steps. The maximum depth of the plastic deformation from MHP required to generate new β-grain orientations was determined by electron backscatter diffraction local average misorientation analysis to be < 0.5 mm, which was less than the melt pool depth in the WAAM process. Nevertheless, new β-grain orientations were observed to form within the peened layer ahead of the approaching heat source as the peak temperature rose above the β transus, which then grew into the less deformed core of the wall as the temperature rose. This allowed the new grain orientations to penetrate deeper than the melt pool depth and survive to act as substrates for epitaxial growth at the fusion boundary during solidification, resulting in significant grain refinement.

https://doi.org/10.1007/s11661-020-05781-6

I. INTRODUCTION

A. *WAAM*

THE near-net-shape production of Ti components by Additive Manufacturing (AM) is particularly advantageous due to the high cost of manufacturing complex Ti parts by the conventional routes of forging or casting, followed by machining. There are currently a variety of high deposition rate Directed-Energy Deposition (DED) AM techniques under development, with one of the most cost-effective being Wire-Arc Additive Manufacture (WAAM).[1] The WAAM process has been developed to specifically target the manufacture of near-net shape, meter-scale, structural components with medium complexity, out of chamber, and with a lower investment in capital equipment. Compared to conventional production methods, WAAM can significantly reduce the lead time, production costs, and material usage, while providing competitive mechanical properties.[1,2]

B. *WAAM Microstructures*

Typical WAAM Ti-6Al-4V (Ti64) microstructures contain large columnar β grains with a strong $\langle 001 \rangle$ fiber texture, aligned close to the build direction, that develops by epitaxial re-growth from the fusion boundary up through multiple layers during deposition of the melt tracks.[3–5] In the WAAM process, following each deposition pass, the solidified material below the fusion zone is heated to above the β-transus temperature to a depth equivalent to that of about 4 to 5 added layers and transforms on cooling to a basket weave lamellar α microstructure, with a small volume fraction of retained β.[6,7] There is also typically a thin layer of grain

J.R. HÖNNIGE is with the Welding Engineering and Laser Processing Centre, Cranfield University, Cranfield, MK43 0AL, UK and also with the Premium Aerotec, Premium AEROTEC GmbH, Riesweg 151-155, 26316 Varel, Germany. A.E. DAVIS, A. HO, J.R. KENNEDY, and P. PRANGNELL are with the Department of Materials, University of Manchester, Manchester, M13 9PL, UK. Contcat e-mail: alec.davis@manchester.ac.uk L. NETO is with the Welding Engineering and Laser Processing Centre, Cranfield University.

Manuscript submitted December 13, 2019.
Article published online May 6, 2020

boundary α which delineates the prior β-grain boundaries. Heat-affected zone (HAZ) bands, associated with a temperature rise from re-heating in the range from above ~ 800 °C to the β-transus temperature (~ 980 °C[6]), are also generated by each heat source pass. The HAZ bands are associated with preferential etching caused by coarsening of the α lamellar and increased solute partitioning, which occurs on re-heating to higher temperatures within the β transus approach curve.[6–10] However, due to the high heating rates (above 500 °C s^{-1}) the actual β transus can be displaced by ~ 20 °C to 30 °C[6,11,12] above the equilibrium β-transus temperature.[13] In single-pass-wide walls, the HAZ bands are seen as horizontal, parallel lines, and the spacing between the HAZ bands is equal to the layer height.[14]

In AM with Ti64, the mechanical properties are affected by the size and morphology of the α-plates, as well as the micro-texture inherited *via* the Burgers Orientation Relationship (BOR) from the normally coarse parent β-grain structure, which controls the effective slip line length.[15–19] The diffusion distance during the $\beta \rightarrow \alpha$ transformation, which is dominated by *V* (as the slowest diffusing species), determines the width of the α lamellae[20–22] when they first transform, but they can be substantially coarsened within HAZ bands by the overlap of thermal fields from subsequent deposition passes.[6] The resultant final scale of the transformation structure is, therefore, a complex function of both the cooling rate in each deposition pass and the thermal cycle experienced by the previously deposited material during re-heating in subsequent deposition passes.[6,21,22] The process parameters and part geometry in WAAM strongly influence the initial cooling rates and subsequent thermal cycling seen in each volume of material and, therefore, strongly influence the properties of components in the as-built condition of AM.[16,23,24]

The above heterogeneities normally found in a conventional WAAM build are also present in all components produced by other DED high deposition rate AM processes with Ti64 and can lead to anisotropy in the mechanical tensile and fatigue properties[14–16,25] and, in particular, a reduction in tensile ductility during transverse loading.[14–16] This behavior has largely been attributed to the influence of the parent, coarse columnar β-grain structure and texture generated during solidification, and its effect on the subsequent α micro-texture following transformation.[16,17] Unfortunately, metallurgical efforts to refine the β-grain size by the addition of inoculants (*e.g.* TiN[26]), or elements that act as growth restrictors (*e.g.* B[27] and C[28]), generally have unwanted side effects that can be detrimental to the mechanical properties and pose issues for scrap recycling and qualification.

C. *Inter-pass Deformation*

Previous work[3] has shown that the application of inter-pass cold working in the WAAM process, by rolling each layer sequentially after it is deposited during building, can be very effective in refining the coarse columnar β-grain structure that is normally produced and greatly reduces the strength of both the α and β textures.[3] The benefits of this are much more isotropic and consistent mechanical properties.[2,29,30] Why inter-pass rolling is so effective in refining the grain structure, when applying relatively low applied plastic strains (< 20 pct), is still the subject of on-going research. However, Donoghue *et al.*[31,32] suggested that deformation and rapid re-heating can cause twinning of the β grains when they re-grow, though this is understood to be normally less favorable in Ti64.[33] In addition, when rolling is applied cyclically to each added layer, it is particularly effective because it breaks up the grain structure in each layer and prevents the competitive re-growth through multiple added layers that is required to produce columnar structures.

Another unexpected observation, which has been recently reported by the current authors,[29,34] is the surprising effectiveness of machine hammer peening (MHP) on β-grain refinement and texture weakening in Ti64 WAAM builds, given the low sub-surface depth of deformation expected for this technique. The grain refinement achieved, although less than that for inter-pass rolling, has again has been shown to be beneficial for providing more isotropic properties.[35–37] A comparison, using β-reconstructed electron backscatter diffraction (EBSD) maps to reveal the β-grain structure and texture from WAAM builds without and with inter-pass peening, is provided in Figure 1. In this example, peening has been applied to the top of every deposited layer along its centerline. (The strain field of the final peening operation at the top of the wall can be inferred from the lack of indexing in the EBSD maps.) The roughly equiaxed β grains produced have a diameter of ~ 1 mm and display a much weaker—near random—texture than in a typical undeformed WAAM build (shown in Figure 1(a)). The extent of the grain refinement obtained by the MHP treatment is surprising, given that the expected depth of plastic deformation during MHP is $\lesssim$ 0.7 mm,[34] which is less than the re-melting depth of the previously deposited layer.[4] Therefore, the surface-deformed layer should have been completely re-melted during the subsequent deposition pass. However, microstructure analysis performed in previous work[34] did not contain any time-resolved information so that it was not possible to see how such a refined grain structure developed.

In the current paper, we have thus performed two experiments to more fully understand the relationship between the sub-surface plastic strain distribution generated by MHP and the temperature field within the WAAM process. This has included: (i) analyzing a wall center-section in side-view following a 'stop-action' frozen melt pool experiment, to reveal the grain structure evolution with time after MHP; and (ii) studying samples where MHP was applied to the side surfaces of a WAAM wall to induce a strain gradient perpendicular to the thermal gradient developed in a final deposition pass. This second method was used to deconvolute the effects of the peak temperature reached from the strain gradient generated by peening. When combined with EBSD analysis of the sub-surface deformation field, and reconstruction of the β-phase, this combined approach

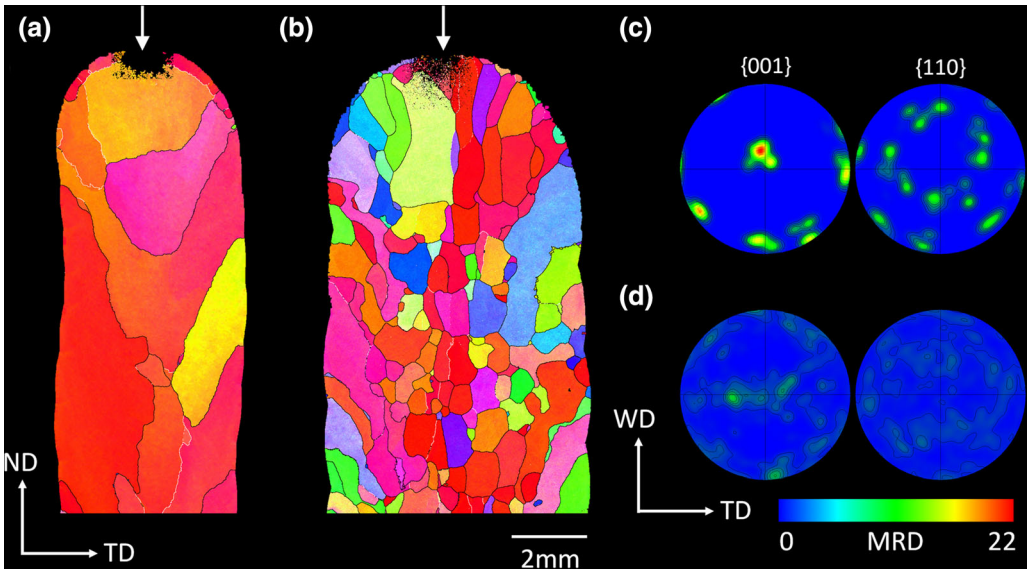

Fig. 1—β-reconstructed EBSD maps of Ti64 WAAM walls (*a*) without and (*b*) with inter-pass MHP, applied to the top surface of each melt track—demonstrating the β-grain refinement that can be achieved. The texture of each wall is provided as pole figures in (*c*) without and (*d*) with MHP, respectively. Peening was applied to every pass along the centerline of the top of the wall in (b) and just to the top of the wall (final pass) in the unrefined build in (a). The depth of high plastic deformation can be inferred from the lack of indexing in the reconstructed maps (arrowed).

Table I. Parameters of Deposition and MHP Process

Ti-6Al-4V Plasma Deposition Parameters				MHP Parameters	
Wire Diameter (mm)	1.2	torch stand-off (mm)	8	tool stand-off (mm)	0.5
Current (A)	145	plasma Gas (l/min)	1	supply pressure (bar)	6
Wire Feed (mm/s)	40	shielding gas (l/min)	10	impact frequency (Hz)	180
Travel Speed (mm/s)	7	trailing gas (l/min)	25	tip radius (mm)	2
				travel speed (mm/s)	36

has allowed a full explanation to emerge for the beneficial grain refinement response seen from the application of surface peening.

II. METHODOLOGY

Two single pass linear WAAM walls were produced for the peening experiments, both consisting of 15 deposited layers, built using an EWM™ plasma power source operating with the parameters provided in Table I. This build height ensured steady-state conditions were achieved; *i.e.* a typical WAAM microstructure was first established before performing the stop-action experiments. The walls were produced with a width of 5.8 mm and layer height of 1.1 mm. A ForgeFix XP™ pneumatic MHP system with a hemispherical WC-coated impact head was used for the surface treatment using the parameters in Table I. This tool operates at 180 Hz and 6 bar was the maximum pressure for the system, with 2 mm the smallest tool radius available, and 0.5 mm the shortest suggested work-piece distance to ensure full lift-off and avoid crashing into the work-piece when translating the tool. This yielded the highest energy density achievable per indent and the maximum plastic deformation depth that could be achieved with this tool. With these parameters, the peening head generated an 80 μm deep by 1.23 mm wide groove in the surface of the Ti64 WAAM parts.[38] A line-pitch of 0.5 mm was therefore enough to guarantee full area coverage. The plasma torch was manipulated with a linear stage and the MHP treatment was applied using a robotic arm. The sample reference frame used throughout is defined as: WD, the heat source travel and wall alignment direction; TD, the wall transverse direction; and ND, the build direction, normal to the deposited layers.

To generate the stop-action samples, a wall was peened with a single end-to-end line along the center of the top of the wall, with the machine head translated at a rate that produced 0.2 mm equidistant indents, as shown in Figure 2(a). An additional layer was then deposited, to re-heat and allow β re-growth within the surface treated previous pass, where the wire feed and arc were stopped half way along the wall—to 'freeze the melt pool'—while in a quasi-steady-state condition.

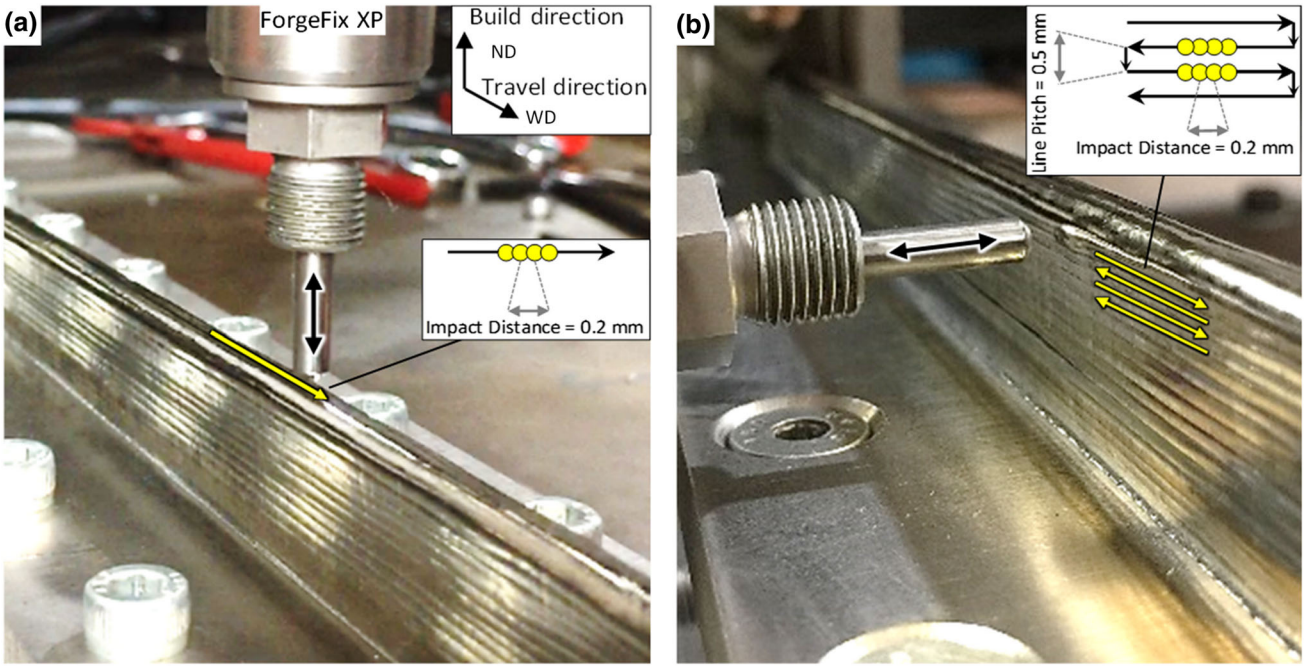

Fig. 2—Application of the MHP surface treatment to Ti64 WAAM walls to produce: (*a*) the WD-ND section stop-action sample, using a single peened line along the wall centerline, and (*b*) the side saturation peened sample.

The second specimen was also built 15 layers high but was peened uniformly on one side. This was achieved by using multiple overlapping tracks, with a lateral off-set of 0.5 mm (Figure 2(b)). In this sample, re-heating and β re-growth were then investigated without adding any more material by just running the plasma arc across the top of the build, which therefore did not change the bead geometry after solidification.

The 'frozen' stop-action sample was sectioned down the wall centerline in the WD-ND plane and metallographically polished for microstructural analysis. With the side peened wall, two cross sections were studied: one after peening and another after the plasma torch heat treatment. Both were viewed in the transverse cross sections (ND-TD plane) taken from the middle of each wall length. Optical microscopy was performed using a Zeiss Axio Imager 2, equipped with image stitching capabilities, after etching in Kroll's Reagent. EBSD was performed on polished samples with an FEI Sirion field emission gun Scanning Electron Microscope (SEM), in conjunction with Oxford Instruments' AZtec software and a Nordlys Nano EBSD detector, using an accelerating voltage of 20 kV and various step sizes, depending on the map area and resolution required. The collected EBSD α orientation data was processed in HKL CHANNEL 5 software. To determine the β-grain structure and texture, reconstruction was performed using the method developed by Davies and Wynne[39,40] (based on References 41 and 42) which involves calculating the most probable parent β orientation from neighboring α orientations, by considering all the possible variants during the $\beta \rightarrow \alpha$ phase transformation, according to the BOR. The EBSD maps below are presented with inverse pole figure coloring (IPF), relative to ND, and texture data is displayed in standard pole figures with intensities given in units of multiples of random density (MRD).

Knowledge of the sub-surface depth of plastic deformation introduced by the peening process was key to understanding its effectiveness; thus, an empirical method was devised to map the strain field generated in the Ti64 WAAM material by MHP using an EBSD misorientation analysis technique. This involved carefully EBSD mapping deformed samples with a step size of 2 μm and using 4 $\times$ 4 frame binning to obtain high -quality local orientation data for the α phase. The orientation data was then converted into local average misorientation (LAM) maps, which calculated the average misorientation, relative to neighboring points in each α lamella, in an 11 $\times$ 11 kernel. The local strain was then determined by calibration against plane-strain compression test samples, for which finite element (FE) modeling was used to estimate the local strain distribution within each sample. To calibrate the effect of strain on the misorientation measurements, 5 mm^3 cube samples were cut from WAAM walls (built identically to those used in this study) and deformed at room temperature in plane-strain compression (using the same methodology as References 31 and 32) to different sample-height reductions. LAM-distance plots, of how the LAM changed across centerline profiles in the sample compression axes, were then extracted from the maps and compared to similar centerline profiles taken from FE simulations of the strain distribution in the plane-strain compression samples, so that LAM and modeled strain data could be correlated at a series of sample positions. From this approach, an empirical relationship could be calibrated between a known cold

deformation strain and the local LAM value in a Ti64 WAAM microstructure. By applying this algorithm to LAM maps, obtained by EBSD of the α phase below a peened surface, strain maps could then be produced and cleaned in ImageJ.[43] It should be noted that strains above 12 pct could not be quantified by this technique as the LAM misorientation within a given α lamella saturated above this point, *i.e.* increasing the strain past 12 pct produced no change in the LAM measurement, so the maximum strain that could be determined in any given map was capped at 12 pct. In addition, in the fine lamellar-α WAAM microstructures investigated, the sensitivity of this EBSD-based method to low strains was restricted to above ~ 4 pct due to noise in the recorded EBSD data. A more detailed description of this technique will be the subject of a future publication.

III. RESULTS AND DISCUSSION

The overall effectiveness of peening each layer on refining the β-grain structure and improving mechanical properties in a built part has already been demonstrated in Figure 1, where the average grain diameter in the peened wall was ~ 1 mm and can be seen to be relatively uniform. Similar results have been shown previously,[29,34–37] but without investigating the mechanisms that allow such surprisingly effective β-grain refinement to occur. It can be seen from Figure 1 that the overall level of grain refinement achieved from applying the MHP technique to the top of each deposited layer is comparable to—but does not quite reach the level of—inter-pass rolling[3,30] where β-grain sizes below 100 μm were obtained. However, the refined MHP grain structure is still greatly improved relative to that seen in the standard WAAM wall (Figure 1(a)) which also has a far stronger β texture.

A. *Quantification of the Deformation Field in Machine Hammer Peening*

In Figure 3, a strain distribution map determined by the EBSD-LAM technique is provided, which shows the typical depth and distribution of the sub-surface deformation induced by a single MHP indent when applied to the top of a WAAM deposition pass. A very steep strain gradient can be seen below the impacted surface. In the near-surface region, the strain was too intense to measure, as EBSD indexing became practically impossible, and the method used to estimate the local strain (described above) broke down for strains above 12 pct. Analysis of the EBSD data did, however, show that the plastic strain fell to below 8 pct at a depth of ~ 500 -600 μm below the tool center, which is understood to be the approximate lower strain limit required to activate β-grain refinement, by producing new β grains that can grow on re-heating Ti64 WAAM with inter-pass deformation.[3,15] This suggests that if peening is applied to the top surface of each track during re-heating, when the next layer is deposited, no new β orientations should be generated at a depth of greater than ~ 0.5 mm below the original surface. In comparison, the depth of re-melting experienced by each layer is shown in Figures 4 and 6 to be ~ 0.7 mm. As will be confirmed below, the depth at which new grains can be nucleated by the MHP process is, therefore, less than that re-melted by each new deposition track, suggesting that all the material deformed to a sufficient strain to generate new β-grain orientations by recrystallisation would have been removed through re-melting when the next layer was deposited. In Figure 3, the EBSD-LAM technique has, however, revealed that lower strain deformation penetrated into the surface to a greater depth, the limit of which was difficult to distinguish with this method, but greater than that previously reported.[34] Owing to the fine nature of the transformation microstructure in the WAAM material, the sensitivity of the EBSD-LAM technique to dislocation accumulation from low strains was approximately 4 pct, and in the map shown, there is evidence that a weaker deformation field extends as deep at least 1 mm below the surface (shown by the black dotted line in Figure 3).

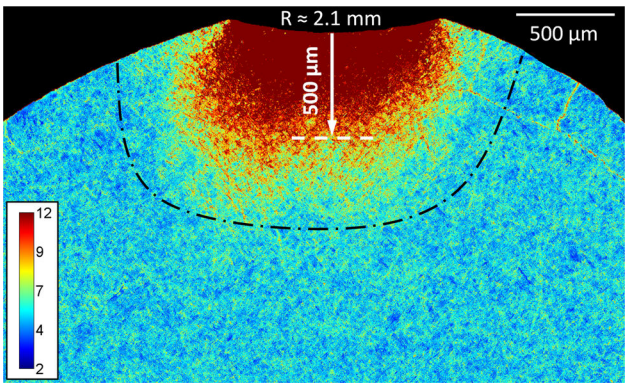

Fig. 3—Sub-surface strain distribution map determined by the EBSD-LAM techniques, showing the depth of deformation induced by MHP in the sample in Fig. 1(a). The strain scale bar is given in percent strain (pct).

B. *The Stop-Action Sample*

A full side section macroscopic view of the stop-action sample is provided in Figure 4, where the process head was traveling from left to right. The wire feed and torch were stopped at the position indicated. The added layer height (LH) has been annotated with a white dotted line. Behind the torch, the HAZ band from the final pass can be seen to have a spacing similar to that generated by the passes used to build the wall below, suggesting the thermal conditions for the final pass were consistent with that experienced in a normal build until the arc was turned off.

It can be seen in Figures 4 and 6, that the depth of re-melting into the previous layer was ~ 0.7 mm. The strain maps in Figure 3 (see Sect. III–A) and Figure 5(a) therefore suggests that all the material deformed by peening to a strain greater than 8 pct would have been re-melted. However, after peening the previous layer and the final deposition pass, behind the stop position of the melt pool (to the left side in Figure 4) a layer with a refined β-grain structure can be seen that has an overall

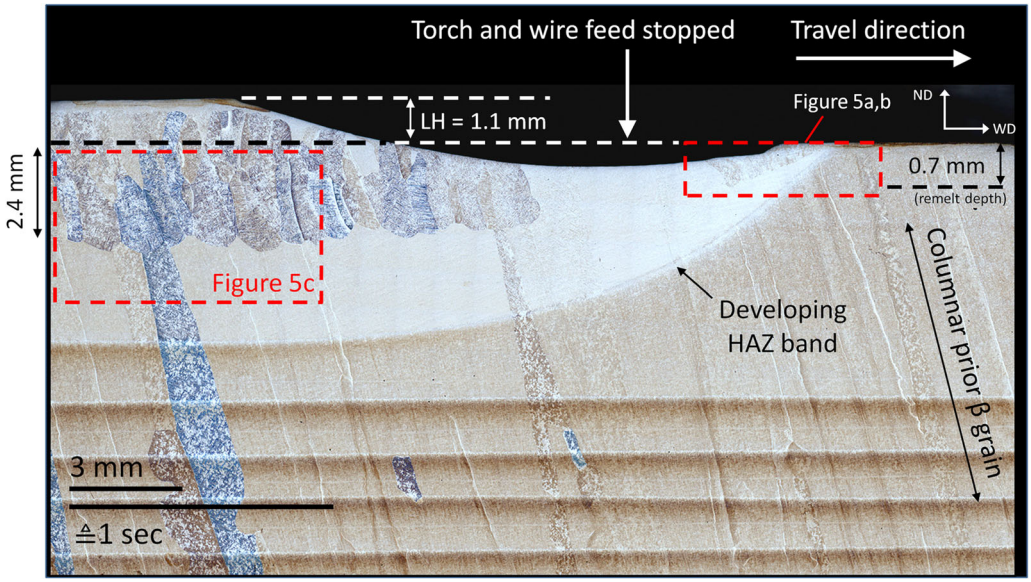

Fig. 4—Macro-view of the 'stop-action' sample showing a section of the wall center-plane through the 'arc-off' position when a final pass was applied after MHP treatment to the top layer, showing the positions of stopping the wire feed and torch, the melt depth, HAZ bands, and non-peened substrate material.

thickness of 3.5 mm. The grains within this layer, while much finer than in the substrate, appear directional, or columnar, in nature and partly grew during solidification of the melt pool, but also extend down to a depth of ~ 2.4 mm below the original position of the peened top surface from the previous pass, which is ~ 1.5 mm below the re-melt depth. This layer therefore includes both grains that grew upwards by solidification from the fusion boundary, and downwards by recrystallisation and grain growth into the low strain region of the deformation zone caused by the peening tool.

In Figure 4, a thin zone of finer recrystallized β grains can also be seen to be forming ahead of the torch stop position. This region has been EBSD mapped in more detail in Figure 5(b). As the heat source first approaches, the peened surface ahead of the moving melt pool will feel the presence of its thermal field and be heated above the β transus before it starts to melt. The α phase will therefore transform back to a full β microstructure, and new, highly misorientated β-grain orientations will be produced to a depth where sufficient prior deformation had been experienced.[3] Once nucleated within the highly strained near-surface layer, these new grain orientations can then grow downwards into the lesser deformed material deeper in the strain field shown in Figure 5(a), until the stored energy provided by peening becomes insufficient. However, the deformation strain required to provide a driving force for grain growth is a lot lower than that needed to create new grain nuclei, so no new grains are formed. This behavior can be seen clearly in Figure 5, where the unindexed points that could not be reconstructed are indicative of the depth of more severe deformation induced by the peening tool. As the torch moves closer, the greater temperature rise increases the growth rate of the newly formed β grains and their recrystallisation front migrates further into the substrate material to a depth which mimics the HAZ band profile, but ultimately will be limited by the extent of strain energy introduced by the peening process. The columnar nature of these grains ahead of the heat source is therefore developed by directional *solid-state* growth within a diminishing strain gradient with depth, caused by the peening process, that is controlled kinetically by the temperature rise within the thermal field of the torch. For this reason, their growth direction is aligned approximately normal to the expected peak temperature isotherms in the heat source thermal field and they grow downwards, tilted towards the heat source travel direction.

As the torch moves further forward and the temperature rises, these new grains then progressively melt (from above) as the melt pool depth increases, but because the new columnar grains that were produced by solid-state recrystallisation have grown downwards sufficiently, they can survive the passage of the melt pool. To illustrate this point, the approximate positions of the melt pool depth and β-transus temperature (determined from the 'refinement boundary') are compared schematically in Figures 5(a) and (b). Once the torch has passed by, the surviving β grains make up the solid surface at the fusion boundary from which epitaxial re-growth will occur during solidification at the rear of the melt pool. In this case, directional growth also occurs producing the finer columnar grains seen behind the frozen melt pool in the left of Figure 4.

The grain structure of the refined layer seen behind the melt pool is magnified in Figure 5(c), which confirms the above interpretation. In this EBSD map, the reconstructed-β grains can be seen to exist within three layers moving from bottom to top: (i) at the base, below the depth of deformation and recrystallisation where there are very coarse grains with a $\langle 001 \rangle$ fiber texture (red in IPF//ND coloring) from the un-peened previously deposited layer, (ii) a thin layer with a weak

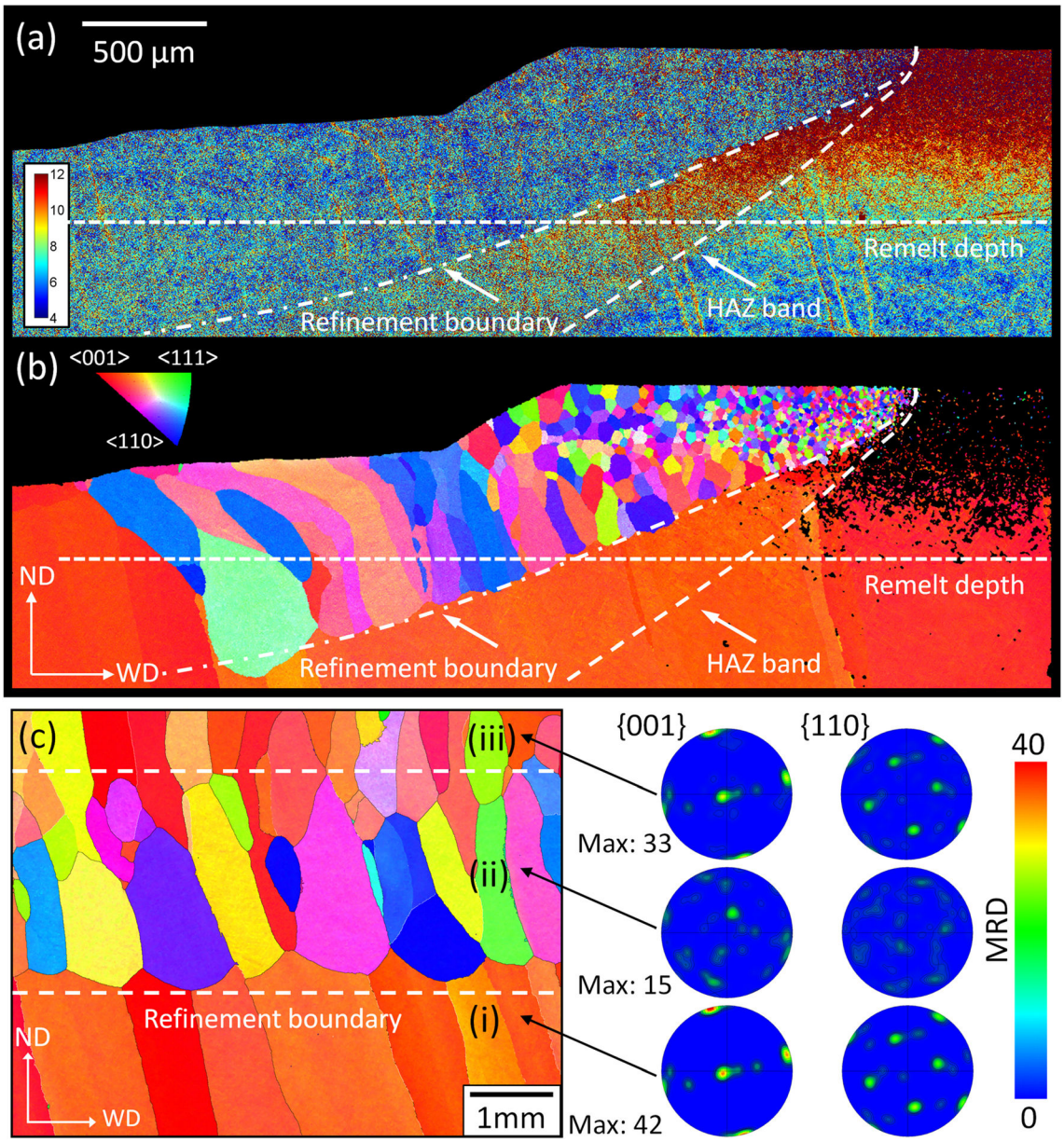

Fig. 5—EBSD maps from the regions shown in Fig. 4 (red dashed boxes) highlighting the behavior of the β-grain structure: (*a*) an EBSD-LAM strain distribution map showing where the thermal field interacts with the MHP plastically deformed material ahead of the approaching melt pool, (*b*) a reconstructed-β map of the same region, and (*c*) a reconstructed-β map from the refined layer seen behind the process head with accompanying pole figures (maximums given in MRD) for each layer.

texture and multiple grain orientations that are the remnants of the recrystallized β grains that grew downwards ahead of the approaching melt pool, and were then mostly melted back from above; and (iii) a final layer of grains above that have nucleated off the surviving recrystallized grains and grown up into the melt pool during solidification. This top layer has a different texture to the band of recrystallized grains and can also be seen to favor a $\langle 001 \rangle$//ND growth direction by the presence of more red grains, as well as the re-emergence of a $\langle 001 \rangle$ fiber component in the accompanying pole figure. However, because only a single melt pass has been solidified, there has not been as much opportunity for growth selection to produce the strong texture and coarser grain structure seen in a conventional build.

C. *HAZ Formation*

In addition to the main discussion regarding the grain structure development, the 'stop-action' experiment has revealed additional interesting thermal field effects that have not been previously reported. In Figure 4, it is possible to see directly the process that creates the parallel HAZ bands seen further down in the build, that have been reported previously.[9,10] The top of the HAZ bands found in Ti64 WAAM deposits has been recently confirmed to coincide with a temperature rise equivalent

to the β-transus temperature, which is shifted to a slightly higher temperature in the WAAM process due to the high heating rate (~ 500 C s^{-1}.[6]) Ahead of the melt pool, the final band curves upwards ahead of the heat source stop position due to the temperature rise when the heat source approaches, in agreement with thermal models of the WAAM process[44]; and behind the heat source, it can be seen to continue as the trailing locus of the position of the β-transus peak temperature isotherm, which is 'drawn on' to the prior transformation microstructure as the heat source advances.

Secondly, near to the 'stop-action' position, in the macrograph in Figure 4, the region that was fully β-annealed in the final heat source pass (*i.e.* above the final HAZ band isotherm) appears with lighter contrast, relative to the previously deposited tracks. This etch contrast effect is not normally seen in post-mortem studies of builds that have not been 'stopped' in-process. However, it is noticeable in Figure 4 that the contrast of the lighter final pass becomes more similar to that for the rest of the build to the left of the image, which is further behind the heat source, and therefore corresponds to a longer thermal exposure. It thus seems likely that, with increasing distance behind the heat source (and greater thermal exposure), greater solute partitioning (probably of V) occurs between the α and β phases, which causes the etch contrast in the final layer to become more similar to that of the previously deposited materials.

D. *Side Peening*

Side peening was applied to a second set of wall samples to investigate the effect of imposing a temperature gradient perpendicular to the MHP strain gradient and therefore deconvolute the effects of temperature from the strain generated by peening. Figure 6 compares cross sections of WAAM walls that were MHP treated over their left hand surfaces, before (Figure 6(a)) and after (Figure 6(b)) re-melting the final deposited layer with one additional heat source pass. In Figure 6(a), the black dashed line represents the bead profile from the previous pass. A faint outline of the fusion boundary can also be observed in each sample as a thin band of slightly darker contrast, which is highlighted by the white dashed line. In WAAM deposits, it was recently shown[6] that this etching contrast is caused by subtle fusion boundary segregation, mainly Fe. In Figure 6(a), four large columnar β grains can be seen growing epitaxially up through multiple deposited layers. The equidistant surface indentations on the left surface of the deposits were caused by the MHP tracks. In the accompanying EBSD data in Figure 7(c), the prior parent β grain in the wall bulk is red in IPF-ND coloration, reflecting the near alignment of the $\langle 001 \rangle$ growth direction with the build direction preferred during solidification, similar to in Figure 1(a).[3] In Figure 6(b), following re-heating by the final heat source pass, new β grains can be seen that have developed from the peened surface of the sample and grown inwards into the wall. It can also be noted that the depth of inward growth and grain size increases with proximity to the top wall surface and, therefore, the peak temperature experienced at each height position. However, it can be noted that no new β grains are found below the position of the top-most HAZ band, which corresponds to the β transus temperature [6].

When viewed in the EBSD maps (Figure 7(c)) and at higher magnification in Figure 7(d), very fine equiaxed β grains are first found to appear on re-heating to peak temperatures equivalent to just above the first HAZ band, or β-transus temperature, but are restricted to a

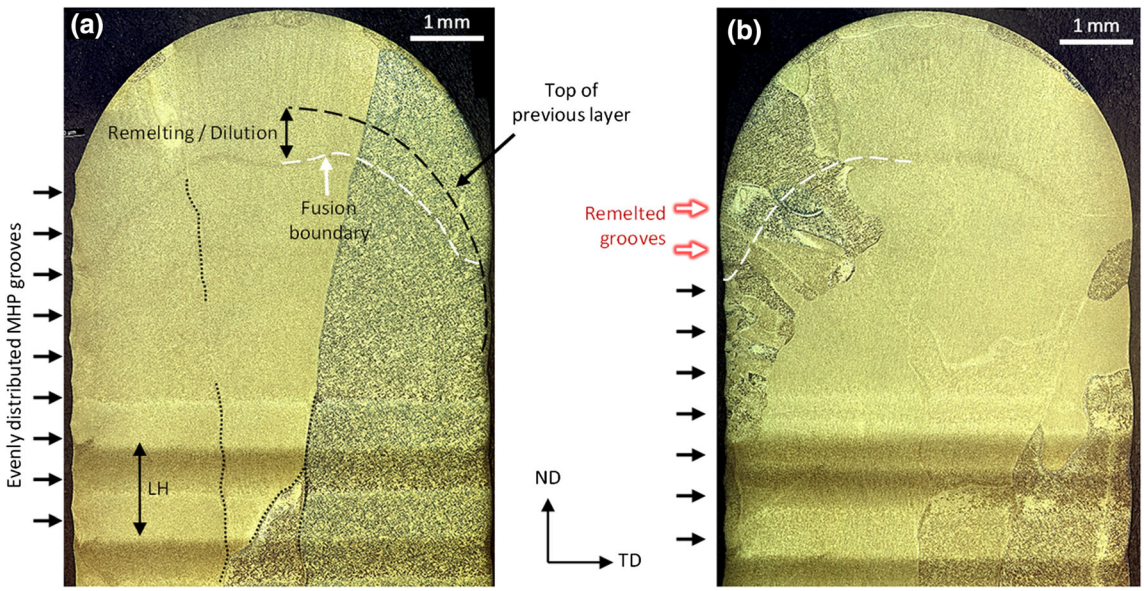

Fig. 6—Macrographs of the transverse (ND-TD) sections from WAAM single-pass-wide walls (*a*) produced conventionally (with no deformation) followed by side peening of the left surface after the sample was built, and (*b*) the same post-deposited side peened wall following re-melting of the top surface with a final heat source only pass.

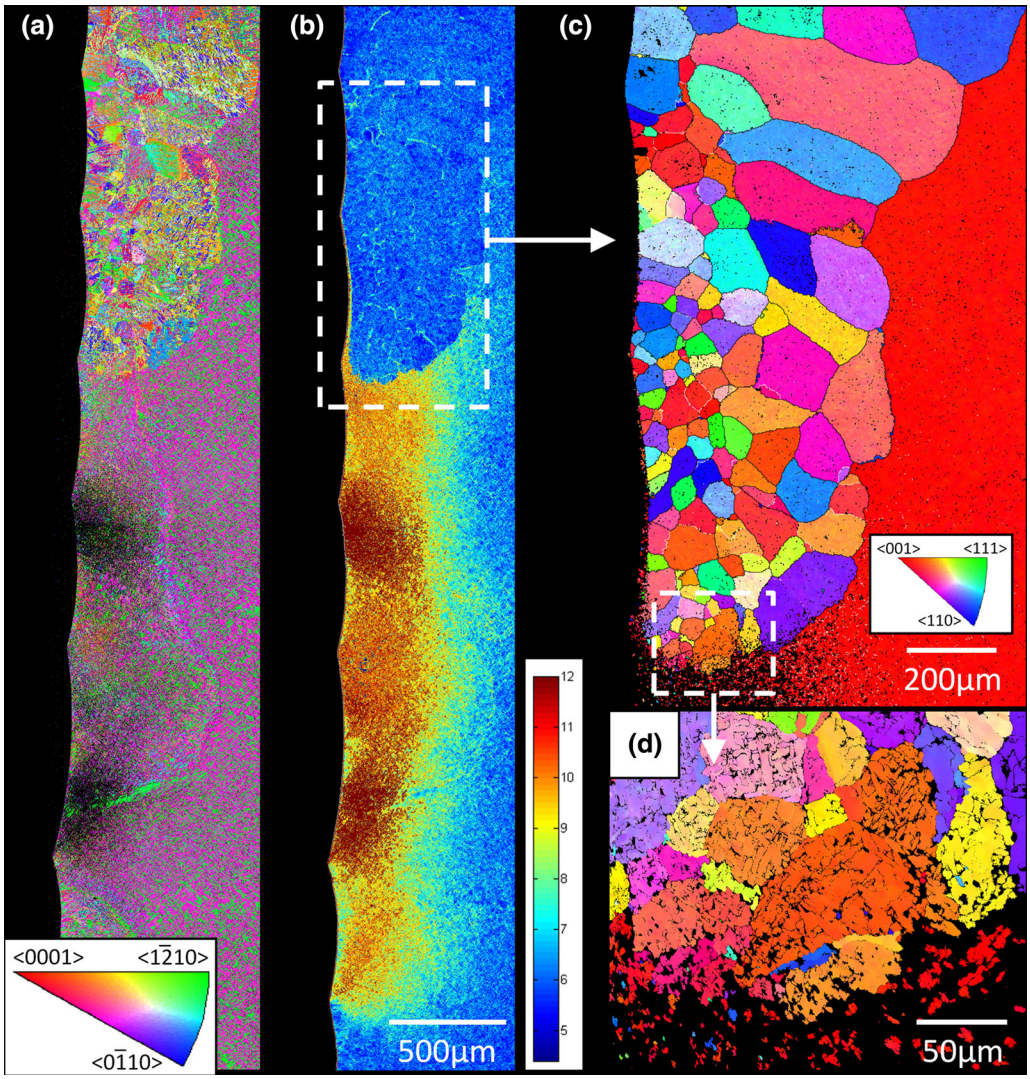

Fig. 7—EBSD maps of the left of the wall after MHP and heat treatment (Fig. 6(b)) showing (*a*) the α phase, (*b*) the EBSD-LAM measured strain (scale in pct), (*c*) the reconstructed-β phase of the recrystallized region, and (*d*) a higher resolution reconstructed-β map of the region highlighted in (c).

shallow depth within the more severe surface deformation layer (Figure 7(b)). With increasing height and peak temperature rise, the new refined β grains can be seen to coarsen (top of Figure 7(c)) and become differentiated between those close to the surface that stay equiaxed, and those further in, which grow inwards into the lesser deformed wall core—where no more grain nucleation occurs—and thus become elongated in the process. In Figure 7(c), the sub-surface depth that new grain orientations can be seen to form is actually quite shallow and less than ~ 500 μm, which corresponds to the heavily strained region of the peened layer shown in Figure 7(b). This situation is thus similar to the new layer of grain nucleation and downwards grain growth seen ahead of the torch, below the top peened stop-action sample discussed in Figure 5.

The depth the grains grow into the wall again increases with the peak temperature reached above the β transus, demonstrating a highly temperature-dependent growth rate. The grains growing inwards rapidly penetrate deeper with height position, extending as far as 2.4 mm at the top of the build, which is a similar depth to that seen behind the heat source in Figure 4. This observation therefore suggests that some strain energy from the peening treatment may be present to a greater depth than could be detected by EBSD (Figure 3) but below 2.4 mm deep this becomes insufficient to drive further grain growth. It can also be seen at the top left of Figure 6(b) that the new β grains that formed by recrystallisation and grew inwards into the wall go on to act as substrates for epitaxial re-growth from the fusion boundary back into the melt pool.

E. *The Effectiveness of β-Grain Refinement by Surface Peening*

The results reported above show that surface mechanical peening has the potential to greatly refine the coarse columnar β-grain structure and the strong texture normally seen in WAAM Ti64 deposits that result from

repeated epitaxial solidification in a moving melt pool, with a low freezing range alloy that contains effectively no melt inoculants. The resultant reduced grain size and weaker texture has been demonstrated to decrease the mechanical anisotropy seen in WAAM components.[2,14,35–37] Importantly, it has been found that grain refinement can be achieved in relatively thick sections, which is surprising given that a surface treatment method like MHP only induces deformation to a limited depth, compared to the melt pool depth and part dimensions.[34] The fact that the MHP process can be successfully used to build fully refined practical section thicknesses is also particularly advantageous as robotic peening is far more flexible than inter-pass rolling[2,3,15,30] and can be applied to more complex build geometries.

EBSD-LAM measurements of the sub-surface strain, induced by the MHP technique employed here, showed it reached undetectable levels below depths of less than ~ 1.5 mm (Figures 3 and 7(b)), whereas grain refinement was found to a depth of ~ 2.4 mm (Figure 4). Importantly, peening was also found to work in circumstances where the depth of re-melting, when the next layer was added, was greater than the depth of surface deformation required to nucleate new β grains by recrystallisation during re-heating through the β transus (Figures 4 and 5). For example, new β orientations were found by Donoghue *et al.*[3] to only form at relatively shallow depths within the peened layer where the plastic strain exceeded at least 8 pct.

Where there was sufficient sub-surface strain, new β grains were observed to form within the surface-deformed layer only for peak temperature rises above the β transus temperature (Figure 7). The mechanisms by which the new β-grain orientations first form within the peened layer have not been investigated here in detail and are the subject of another publication.[32] However, to refine the grain size, new β-grain orientations must be generated as a result of the deformation induced by the surface peening process, and/or when the β phase re-grows during the $\alpha \rightarrow \beta$ transformation. Parallel studies[32] on the origin of the relatively low plastic strain required to obtain high levels of β-grain refinement in WAAM inter-pass rolling have used simulations and rapid heating experiments to investigate the refinement mechanism in more detail. This work suggests that, under the unusual rapid heating conditions present in the WAAM process, some new grain orientations originate from heterogeneities within the deformed state, such as at prior β-grain boundaries, but other grain orientations can also arise from deformation-induced annealing twinning. The high strain rate and complex, overlapping deformation fields induced by the peening process may also be beneficial in this respect.

Taken together, analysis of the stop-action and side peening samples can be used to explain the surprising observation that the grain refining effect from surface peening is not wiped out by re-melting of the thin peened layer. These experiments have shown that peening is more successful than expected because the new β grains produced by recrystallisation, in the heavily deformed near-surface layer, go on to grow rapidly further downwards into the core of a wall (Figures 4 and 5), and therefore penetrate deeper than the melt pool depth. They are thus able to survive re-melting to act as epitaxial substrates at the fusion boundary during subsequent solidification at the rear of the melt pool. Although the thermal cycle is short in AM, grain growth is known to be unusually fast in Ti alloys above the β-transus temperature and will be extremely rapid at temperatures approaching the fusion boundary.[45–47] For example, in Figures 5(b) and 7(c) and (d), it can be seen that in the peened surface layer, the refined β-grain size just above the first HAZ band, where the temperature experienced that gave rise to a full β structure was lowest, is ≤ 20 μm, whereas the grains grew in size to ~ 1 mm by the top of the sample. A downside of this rapid grain growth is, however, that it leads to a coarser final β-grain size. It may therefore be possible to reduce the final grain size by optimizing the process parameters. For example, increasing the heat source travel speed will affect the time available for grain growth as the heat source approaches.

Finally, MHP is more successful when applied repeatedly to every deposited track, as shown in Figure 1, than in single layer experiments. This occurs partly because, when top surface peening is employed, the grains that develop during solidification grow off the layer of recrystallized grains produced below the fusion boundary, that already have a weak texture (Figure 5(b)), but also because the new grains are only able to grow back through one melt layer before they are re-deformed. Therefore, solidification does not occur with the same grains re-growing each time through the many deposited layers required for grain selection to develop the pronounced columnar structure, or strong solidification texture seen in a conventional build; *i.e.* in an iterative process where peening is applied to every deposition pass, new β grains are nucleated cyclically in every layer with a weakened texture, that grows into the previously deposited layer, to act as nuclei for the grains that then solidify in the melt pool and already have a weak texture before being subjected to the next MHP surface treatment, as deposition repeats. Eventually, a steady state is therefore reached producing grains of ~ 1 mm in diameter, which is probably limited by the grain growth that occurs on re-heating each layer, but a strong texture is not allowed to develop. In contrast, in a normal undeformed WAAM build, the opposite takes place in that the β grains re-grow with the same parent orientation in each pass when they are re-heated above the β transus temperature. In the conventional process, under steady-state conditions, growth selection of favorably orientated β grains is thus allowed to occur and increase over multiple deposition cycles, leading to the strong $\langle 001 \rangle$ // ND fiber textures and coarse grain structures that are exemplified in the undeformed bulk wall shown in Figure 1(a).

IV. CONCLUSIONS

This study has shown that robotic machine hammer peening (MHP) has the potential to refine the coarse, columnar, β-grain structures and strong textures

normally found with the WAAM process in Ti alloys like Ti-6Al-4V. When surface peening was applied to every deposited layer, the conventional centimeter-scale columnar β-grain structure was successfully refined to produce an equiaxed structure with an average grain diameter of ~ 1 mm and a weak texture. Importantly, it has been shown that this can be achieved despite the limited deformation penetration depth of peening, relative to the large melt pool depth inherent to high deposition rate AM processes like WAAM, and can reduce the mechanical anisotropy found in full-scale WAAM components.

The 'stop-action' and side peening experiments revealed that the depth of deformation induced by MHP, required to produce new β-grain orientations, was restricted to a sub-surface layer that had experienced greater than ~ 8 pct plastic strain. This occurred to a depth of only 0.5 mm, which was less than the re-melt depth (~ 0.7 mm). However, the new β-grain orientations were observed to first develop within the peened surface layer ahead of the advancing heat source. The new recrystallized β-grain orientations, produced in the heavily deformed near-surface layer, were then able to grow significantly further below the peened surface as the temperature rose higher into the β-phase field. This allowed the new grains to penetrate deeper than the melt pool depth and thus survive re-melting, to act as nuclei at the fusion boundary where they reduced the grain size during solidification at the rear of the moving melt pool. Lower levels of sub-surface deformation were detected by EBSD to a greater depth of 1–1.5 mm, and peening appeared to have provided sufficient stored energy to drive grain growth of the new β-grains to about 2.4 mm below the peened surfaces, which was the limit of the depth of penetration.

The limited depth of the strain available from surface peening, relative to the melt pool depth, therefore meant that some grain growth was required to preserve its benefits, and this also leads to a coarser β-grain size than can be achieved by alternative deformation techniques for refining the grain structures in DED AM processes, such as inter-pass rolling. However, robotic peening is far easier to implement than inter-pass rolling and is more versatile in terms of the part geometries to which it can be applied.

ACKNOWLEDGMENTS

The authors are appreciative of the EPSRC (Grants NEWAM – EP/R027218/1; LightForm - EP/R001715/1), Innovate UK (Open Architecture Additive Manufacturing, OAAM), the European AMAZE Project (No. 313781), and the Advanced Metallic Systems CDT (Grant No. EP/L016273/1) for supporting aspects of this research, and are grateful to Matthias Kranz at KWM tools GmbH for providing the ForgeFix XP MHP tool. P.B. Prangnell is also grateful to the Royal Academy of Engineering, UK, and Airbus for supporting this research through the Airbus-University of Manchester Centre for Metallurgical Excellence.

OPEN ACCESS

REFERENCES

1. S.W. Williams, F. Martina, A.C. Addison, J. Ding, G. Pardal, and P.A. Colegrove: *Mater. Sci. Technol.*, 2016, vol. 32, pp. 641–47.
2. P.A. Colegrove, J. Donoghue, F. Martina, J. Gu, P.B. Prangnell, and J.R. Hönnige: *Scripta Mater.*, 2017, vol. 135, pp. 111–18.
3. J. Donoghue, A.A. Antonysamy, F. Martina, P.A. Colegrove, S.W. Williams, and P.B. Prangnell: *Mater. Charact.*, 2016, vol. 114, pp. 103–14.
4. S. Rios Contesse: *Cranfield University*, 2017.
5. C. Charles and N. Jarvstrat: in *Proc. 8th Int. Conf. Trends Weld. Res.*, 2009, pp. 477–85.
6. A. Ho, H. Zhao, J.W. Fellowes, F. Martina, A.E. Davis, and P.B. Prangnell: *Acta Mater.* https://doi.org/10.1016/j.actamat.2018.12.038.
7. H. Zhao, A. Ho, A.E. Davis, A.A. Antonysamy, and P.B. Prangnell: *Mater. Charact.*, 2019, vol. 147, pp. 131–45.
8. P.A. Kobryn and S.L. Semiatin: *J. Mater. Process. Technol.*, 2003, vol. 135, pp. 330–9.
9. S.M. Kelly and S.L. Kampe: *Metall. Mater. Trans. A*, 2004, vol. 35A, pp. 1869–79.
10. S.M. Kelly and S.L. Kampe: *Metall. Mater. Trans. A*, 2004, vol. 35A, pp. 1861–7.
11. J.W. Elmer, T.A. Palmer, and J. Wong: *J. Appl. Phys.*, 2003, vol. 93, pp. 1941–7.
12. J.W. Elmer, T.A. Palmer, S.S. Babu, W. Zhang, and T. DebRoy: *J. Appl. Phys.*, 2004, vol. 95, pp. 8327–39.
13. F. Martina, J. Mehnen, S.W. Williams, P.A. Colegrove, and F. Wang: *J. Mater. Process. Technol.*, 2012, vol. 212, pp. 1377–86.
14. F. Wang, S.W. Williams, P.A. Colegrove, and A.A. Antonysamy: *Metall. Mater. Trans. A Phys. Metall. Mater. Sci.*, 2013, vol. 44, pp. 968–77.
15. F. Martina, S.W. Williams, and P.A. Colegrove: in *Proc. SFF Symp.*, 2013, pp. 490–6.
16. P. Åkerfeldt, M.L. Antti, and R. Pederson: *Mater. Sci. Eng. A*, 2016, vol. 674, pp. 428–37.
17. P. Åkerfeldt, M.H. Colliander, R. Pederson, and M.L. Antti: *Mater. Charact.*, 2018, vol. 135, pp. 245–56.
18. G. Lütjering and J.C. Williams: *Titanium*, Springer, New York, 2007.
19. H. Galarraga, R.J. Warren, D.A. Lados, R.R. Dehoff, and M.M. Kirka: *Eng. Fract. Mech.*, 2017, vol. 176, pp. 263–80.
20. J.W. Elmer, T.A. Palmer, S.S. Babu, and E.D. Specht: *Mater. Sci. Eng. A*, 2005, vol. 391, pp. 104–13.
21. G. Lütjering: *Mater. Sci. Eng. A*, 1998, vol. 243, pp. 32–45.

22. R. Filip, K. Kubiak, W. Ziaja, and J. Sieniawski: *J. Mater. Process. Technol.*, 2003, vol. 133, pp. 84–9.
23. B. Baufeld, E. Brandl, and O. Van Der Biest: *J. Mater. Process. Technol.*, 2011, vol. 211, pp. 1146–58.
24. B.K. Foster, A.M. Beese, J.S. Keist, E.T. McHale, and T.A. Palmer: *Metall. Mater. Trans. A*, 2017, vol. 48, pp. 4411–22.
25. X. Zhang, F. Martina, J. Ding, X. Wang, and S.W. Williams: *Fatigue Fract. Eng. Mater. Struct.*, 2017, vol. 40, pp. 790–803.
26. D. Qiu, D. Zhang, M.A. Easton, D.H. St John, and M.A. Gibson: *Metall. Mater. Trans. A*, 2018, vol. 49A, pp. 1444–9.
27. M.J. Bermingham, D. Kent, H. Zhan, D.H. Stjohn, and M.S. Dargusch: *Acta Mater.*, 2015, vol. 91, pp. 289–303.
28. S. Mereddy, M.J. Bermingham, D. Kent, A. Dehghan-Manshadi, D.H. StJohn, and M.S. Dargusch: *JOM*, 2018, vol. 70, pp. 1670–6.
29. J. Donoghue, J. Sidhu, and A. Wescott: *TMS Annu. Meet.*, 2015, vol. 2015, pp. 437–44.
30. F. Martina, P.A. Colegrove, S.W. Williams, and J. Meyer: *Metall. Mater. Trans. A*, 2015, vol. 46A, pp. 6103–18.
31. J. Donoghue: *Thesis*, 2016, p. 201.
32. J. Donoghue, A.E. Davis, C.S. Daniel, A. Garner, F. Martina, J. Quinta da Fonseca, and P.B. Prangnell: *Acta Mater.*, 2019, vol. 186, pp. 229–41.
33. S. Hanada and O. Izumi: *Metall. Trans. A*, 1986, vol. 17, pp. 1409–20.
34. J.R. Hönnige, P.A. Colegrove, and S. Williams: *Procedia Eng.*, 2017, vol. 216, pp. 8–17.
35. J.-G. Byun, H. Yi, and S.-M. Cho: *J. Weld. Join.*, 2017, vol. 35, pp. 6–12.
36. Y. Yang, X. Jin, C. Liu, M. Xiao, J. Lu, H. Fan, and S. Ma: *Metals (Basel)*, 2018, vol. 8, p. 934.
37. L. Neto, S. Williams, J. Ding, J. Hönnige, and F. Martina: *Advanced Surface Enhancement*, Springer Singapore, Singapore, 2020.
38. J.R. Hönnige: *Cranfield University*, 2018.
39. P.S. Davies: *University of Sheffield*, 2009.
40. P.S. Davies, B.P. Wynne, W.M. Rainforth, M.J. Thomas, and P.L. Threadgill: *Metall. Mater. Trans. A Phys. Metall. Mater. Sci.*, 2011, vol. 42, pp. 2278–89.
41. M. Humbert and N. Gey: *J. Appl. Crystallogr.*, 2002, vol. 35, pp. 401–5.
42. N. Gey and M. Humbert: *J. Mater. Sci.*, 2003, vol. 38, pp. 1289–94.
43. C.A. Schneider, W.S. Rasband, and K.W. Eliceiri: *Nat. Methods*, 2012, vol. 9, pp. 671–5.
44. X. Bai, P.A. Colegrove, J. Ding, X. Zhou, C. Diao, P. Bridgeman, J. Roman Hönnige, H. Zhang, and S.W. Williams: *Int. J. Heat Mass Transf.*, 2018, vol. 124, pp. 504–16.
45. A.L. Pilchak, G.A. Sargent, and S.L. Semiatin: *Metall. Mater. Trans. A Phys. Metall. Mater. Sci.*, 2018, vol. 49, pp. 908–19.
46. S.L. Semiatin, J.C. Soper, and I.M. Sukonnik: *Acta Metall.*, 1996, vol. 44, pp. 1979–86.
47. O.M. Ivasishin, S.L. Semiatin, P.E. Markovsky, S.V. Shevchenko, and S.V. Ulshin: *Mater. Sci. Eng. A*, 2002, vol. 337, pp. 88–96.